

# Complex Scalar Singlet Model: Electroweak Phase Transition and Gravitational Waves

---

**Dilip Kumar Ghosh, Debadrita Mukherjee, Koustav Mukherjee, and Rohan Pramanick**

*School of Physical Sciences, Indian Association for the Cultivation of Science, Kolkata-700032, India*

*E-mail:* [dilipghoshjal@gmail.com](mailto:dilipghoshjal@gmail.com), [mukherjeedebadrita531@gmail.com](mailto:mukherjeedebadrita531@gmail.com),  
[koustav.physics1995@gmail.com](mailto:koustav.physics1995@gmail.com), [rohanpramanick25@gmail.com](mailto:rohanpramanick25@gmail.com)

**ABSTRACT:** The Standard Model (SM) cannot explain the observed baryon asymmetry of the Universe (BAU), thus driving the need for physics beyond the SM, which can generate electroweak baryogenesis through a strong first-order electroweak phase transition (SFOPT). We extend the SM with a complex singlet scalar (cxSM) and examine the phase transition behavior using a fully general renormalizable scalar potential that permits a complex vacuum expectation value for the singlet and coupled dynamics among multiple scalar fields. Employing the one-loop thermal effective potential with daisy resummation and appropriate counter terms, we conduct an extensive scan of the parameter space, enforcing both theoretical and experimental limits on the scalar sector. This analysis reveals viable domains yielding SFOPT. From these regions, we select representative benchmark scenarios demonstrating multi-stage transitions, producing stochastic gravitational wave signals via bubble nucleation dynamics. The resulting spectra lie within the projected sensitivity of next-generation observatories, including LISA, BBO, DECIGO, and U-DECIGO. Thus, the cxSM offers a compelling setting for electroweak baryogenesis, enriched by correlated gravitational-wave and collider phenomenology.

---

## Contents

<b>1</b>	<b>Introduction</b>	<b>1</b>
<b>2</b>	<b>Model</b>	<b>2</b>
2.1	Scalar potential	2
2.2	Constraints	4
<b>3</b>	<b>Phase transition</b>	<b>8</b>
3.1	Effective potential	8
3.2	Scan based analysis	10
3.3	Types	12
<b>4</b>	<b>Gravitational waves</b>	<b>14</b>
<b>5</b>	<b>Conclusion and discussion</b>	<b>18</b>
<b>A</b>	<b>Lagrangian parameters in terms of physical quantities</b>	<b>20</b>
<b>B</b>	<b>Counter terms in the effective potential</b>	<b>20</b>

---

## 1 Introduction

The origin of the observed Baryon Asymmetry of the Universe (BAU) [1] remains one of the fundamental mysteries that currently lacks a viable description within the Standard Model (SM) of particle physics, despite its tremendous success. This remains one of the key motivations for pursuing physics beyond the Standard Model (BSM), apart from the non-explanation of tiny neutrino mass and the existence of dark matter (DM). The dynamical generation of such an asymmetry requires one to meet the three Sakharov conditions, i.e, the violation of baryon number, the existence of C and CP violating processes, and the departure from thermal equilibrium [2]. The SM can account for the CP-violating processes, although their contribution turns out to be minuscule compared to observational evidence. Additionally, the electroweak symmetry breaking phase transition is a smooth crossover [3, 4] with the observed Higgs boson mass, excluding the possibility of electroweak baryogenesis [5–8] in the context of the SM alone.

The strong first order phase transition (SFOPT) provides a viable framework to satisfy the necessary condition for processes to go out of equilibrium. In addition, SFOPT can generate signatures of stochastic gravitational waves (GW) that can be probed in various experiments, such as the upcoming space-based interferometers, such as LISA [9], BBO [10, 11], DECIGO, and U-DECIGO [12, 13]. These offer a novel and complementary probe to investigate various BSM scenarios.

The simplest possible scenario to achieve an SFOPT is to consider a gauge singlet scalar extension of the SM [14, 15], which has been studied extensively in the literature for various phenomenological studies, which include collider searches [16], production of GWs [17], and electroweak baryogenesis [18]. Apart from that, this setup also allows a possible dark matter candidate stabilized by an additional discrete or continuous global symmetry. In addition, inclusion of additional scalar doublets and other well-motivated gauge extended BSM scenarios have also been explored to achieve SFOPT [19–24].

In this work, we explore the dynamics of phase transition in a complex gauge singlet extension of the SM, considering the most general scalar potential without any additional symmetry imposition on the singlet, usually referred to as the “cxSM”. Inclusion of non self-hermitian terms in the scalar potential with all real couplings allows a vacuum configuration with the complex vev of the singlet. The complex phase of singlet vev can also violate CP spontaneously in the presence of additional heavy Majorana fields [25, 26] or non-renormalizable fermionic interactions to drive electroweak baryogenesis (EWBG) [18]. We focus on the dynamics of the SFOPT involving three fields, i.e, the real and imaginary parts of the scalar singlet along with the SM Higgs, which serves as an essential requirement to study EWBG in cxSM, while refraining from a dedicated analysis of EWBG, which we defer for a future work. We also discuss the generated GWs from SFOPT and their detection prospects in near future detectors.

The draft is organized as follows. In section 2, we describe the complex singlet extended SM, briefly mentioning the relevant theoretical as well as experimental constraints. We construct the effective potential in section 3 and discuss the details of SFOPT via several benchmark points. The stochastic GW spectrum generated for the benchmark points is presented in section 4 before finally concluding in section 5.

## 2 Model

The cxSM is the simplest scalar extension in which the scalar sector of the SM is augmented with a single complex singlet gauge scalar ( $S$ ) [27]. To remain self-consistent, we discuss the scalar potential along with the most general vacuum configuration, highlighting all the relevant constraints on the couplings in the following subsections.

### 2.1 Scalar potential

Along with the SM Higgs doublet ( $H$ ), the most general renormalizable potential of the cxSM at the tree level can be decomposed as

$$V_0(H, S) = V_{\text{SM}} + V_S + V_{HS}, \quad (2.1)$$

where  $V_{\text{SM}}$  is the SM contribution,  $V_S$  constitutes all possible cubic and quartic self interactions of  $S$ , while the interactions of the scalar singlet with the Higgs doublet are

encapsulated in  $V_{HS}$ . Individual contributions are given by

$$\begin{aligned}
V_{\text{SM}} &= -\frac{1}{2}\mu_H^2 H^\dagger H + \frac{1}{4}\lambda (H^\dagger H)^2, \\
V_S &= \left( aS + \frac{1}{4}b_1 S^2 + \text{h.c.} \right) + \frac{1}{2}b_2 |S|^2 + \left( \frac{1}{6}\mu_3 S^3 + \tilde{\mu}_3 |S|^2 S + \text{h.c.} \right) \\
&\quad + \left( \frac{1}{8}d_1 S^4 + \frac{1}{8}d_3 |S|^2 S^2 + \text{h.c.} \right) + \frac{1}{4}d_2 |S|^4, \\
V_{HS} &= H^\dagger H \left[ \left( \frac{1}{4}\delta_1 S + \frac{1}{4}\delta_3 S^2 + \text{h.c.} \right) + \frac{1}{2}\delta_2 |S|^2 \right].
\end{aligned} \tag{2.2}$$

The coefficients of non-self hermitian terms arising in Eq. 2.2 can, in general, be complex; however, we choose all the couplings to be real for simplicity. The linear term can be eliminated by a constant shift in the scalar field  $S$ ; however, we keep all terms without further redefinition of cubic and quartic terms upon field shift [28]. Additionally, imposition of various discrete or continuous global symmetries on the additional scalar singlet required for different phenomenological studies of interest can drastically reduce the number of terms. Nevertheless, we work with the full potential given in Eq. 2.1 without the imposition of any *ad hoc* symmetry by hand. It is important to note that the scalar potential defined in terms of  $H$  and  $S$  is different from that of two real scalar singlet extensions due to the inherent  $\mathbb{Z}_2$  symmetry under which the complex scalar transforms into  $S \rightarrow S' = S^*$ . In terms of their components, the scalar fields can be represented as

$$H = \begin{pmatrix} G^+ \\ \frac{1}{\sqrt{2}}(h + iG^0) \end{pmatrix} ; \quad S = \frac{1}{\sqrt{2}}(s_r + i s_i), \tag{2.3}$$

where  $s_r(s_i)$  indicates the real (imaginary) components of the scalar singlet,  $G^+(G^0)$  represents the charged (neutral) Goldstone boson, while  $h$  is the real part of the neutral component of the scalar doublet. The vacuum expectation values (vev) of the corresponding fields are given as

$$\langle h \rangle = v_h \quad ; \quad \langle s_r \rangle = v_r \quad ; \quad \langle s_i \rangle = v_i. \tag{2.4}$$

It is important to note that in the presence of non-self hermitian couplings in the scalar potential defined in Eq. 2.1, the scalar singlet can obtain a complex vev, which is the most general vacuum configuration possible within this setup. The minimization conditions for the aforementioned vev configurations are given as

$$\mu_H^2 = \frac{1}{2} \left[ \sqrt{2}v_r\delta_1 + v_i^2(\delta_2 - \delta_3) + v_r^2(\delta_2 + \delta_3) + \lambda v_h^2 \right], \tag{2.5}$$

$$\begin{aligned}
b_1 &= \frac{1}{24v_r} \left[ -24\sqrt{2}a_1 + 6\sqrt{2}\mu_3(v_i^2 - 3v_r^2) - 2\sqrt{2}\tilde{\mu}_3(v_i^2 + v_r^2) - 3\sqrt{2}v_h^2\delta_1 \right. \\
&\quad \left. - 6v_r(4d_1(v_r^2 - v_i^2) + d_3(v_r^2 + v_i^2) + 2v_h^2\delta_3) \right],
\end{aligned} \tag{2.6}$$

$$b_2 = \frac{1}{24v_r} \left[ -24\sqrt{2}a_1 + 6\sqrt{2}\mu_3(v_i^2 + v_r^2) - 2\sqrt{2}\tilde{\mu}_3(v_i^2 + 5v_r^2) - 3\sqrt{2}v_h^2\delta_1 \right]$$

$$+ 6v_r((2d_1 - 2d_2 + d_3)v_i^2 + (2d_1 - 2d_2 - d_3)v_r^2 - 2v_h^2\delta_2) \Big]. \quad (2.7)$$

We now proceed to discuss the mass spectrum of the neutral scalars, which is an essential ingredient for the study of phase transitions. In the absence of well defined CP eigenstates, the neutral squared mass matrix  $\mathcal{M}_0^2$  is a symmetric  $3 \times 3$  Hermitian matrix that can be written on the basis  $(h \ s_r \ s_i)^\top$  and is given by

$$\mathcal{M}_0^2 = \begin{pmatrix} \frac{1}{2}\lambda v_h^2 & \frac{1}{4}v_h(\sqrt{2}\delta_1 + 2v_r(\delta_2 + \delta_3)) & \frac{1}{2}v_h v_i(\delta_2 - \delta_3) \\ \cdot & \frac{1}{24v_r} \left[ -24\sqrt{2}a_1 + 6\sqrt{2}c_{12}v_r^2 + 12d_{123}v_r^3 + \sqrt{2}((6\mu_3 - 2\tilde{\mu}_3)v_i^2 - 3v_h^2\delta_1) \right] & \frac{1}{6}v_i \left[ \sqrt{2}(-3\mu_3 + \tilde{\mu}_3) + 3(-3d_1 + d_2)v_r \right] \\ \cdot & \cdot & \frac{1}{2}(d_1 + d_2 - d_3)v_i^2 \end{pmatrix},$$

where  $c_{12} = \mu_3 + \tilde{\mu}_3$  and  $d_{123} = d_1 + d_2 + d_3$ . The squared mass matrix can be diagonalized by an orthogonal transformation to obtain the masses of the physical eigenstates ( $H_1, H_2$ , and  $H_3$ ) through

$$O^\top \mathcal{M}_0^2 O = \text{diag}(M_1^2, M_2^2, M_3^2), \quad (2.8)$$

where  $M_i^2$  is the (mass)<sup>2</sup> of  $H_i$  for  $i = 1, 2$  and  $3$ . The orthogonal matrix relates the gauge and mass eigenbasis by  $(H_1 \ H_2 \ H_3)^\top = O(h \ s_r \ s_i)^\top$  and is constructed as

$$O = \begin{pmatrix} 1 & 0 & 0 \\ 0 & c_1 & s_1 \\ 0 & -s_1 & c_1 \end{pmatrix} \begin{pmatrix} c_2 & 0 & s_2 \\ 0 & 1 & 0 \\ -s_2 & 0 & c_2 \end{pmatrix} \begin{pmatrix} c_3 & s_3 & 0 \\ -s_3 & c_3 & 0 \\ 0 & 0 & 1 \end{pmatrix}, \quad (2.9)$$

with the short-hand notation for the three mixing angles given as  $c_i \equiv \cos \theta_i$  and  $s_i \equiv \sin \theta_i$  for  $i = 1, 2$  and  $3$ .

Using the minimization conditions as given in Eqs. 2.5, 2.6, and 2.7, along with trading all the quartic couplings in terms of physical masses and mixing angles as given in Appendix A, we are left with 13 input parameters for the numerical analysis

$$\{M_1, M_2, M_3, \theta_1, \theta_2, \theta_3, v_h, v_r, v_i, a, \delta_1, \mu_3, \tilde{\mu}_3\}, \quad (2.10)$$

where  $v_h = 246$  GeV and  $M_1 = 125$  GeV are kept fixed throughout the analysis, along with the remaining 11 free parameters.

## 2.2 Constraints

In this section, we discuss various theoretical and experimental constraints that were employed throughout the analysis. The theoretical constraints on the parameters of the scalar potential given in Eq. 2.1 are now in order.

**Unitarity :** Tree-level unitarity of different  $2 \leftrightarrow 2$  scattering processes places constraints on the parameters of the scalar potential and has been extensively studied in the literature

for the SM as well as for various extended scalar sector scenarios. Scatterings of massive gauge bosons can also be taken into account by replacing their longitudinal modes with their corresponding Goldstone bosons, utilizing the high energy limit of the equivalence theorem [29]. Moreover, scalar-scalar interactions are dominated by only their quartic interactions, and the analysis has been performed on the gauge basis as given in Eq. 2.3 due to the simpler form of the quartic couplings. The  $2 \leftrightarrow 2$  scalar scattering processes leads to the  $16 \times 16$  S-matrix, which can be further decomposed into five block diagonal submatrices consisting of three  $\mathcal{M}_1(4 \times 4)$ ,  $\mathcal{M}_2(5 \times 5)$ ,  $\mathcal{M}_3(2 \times 2)$  zero-charged channels,  $\mathcal{M}_4(4 \times 4)$  singly-charged channels and a unique  $\mathcal{M}_1(1 \times 1)$  doubly-charged channel.

The submatrix  $\mathcal{M}_1$  corresponds to the scattering of the initial and final states of any of the states  $\{hs_i, G^0 s_r, G^0 s_i, hs_r\}$  and is given by

$$\mathcal{M}_1 = \begin{pmatrix} \frac{1}{2}(\delta_2 - \delta_3) & 0 & 0 & 0 \\ 0 & \frac{1}{2}(\delta_2 + \delta_3) & 0 & 0 \\ 0 & 0 & \frac{1}{2}(\delta_2 - \delta_3) & 0 \\ 0 & 0 & 0 & \frac{1}{2}(\delta_2 + \delta_3) \end{pmatrix}, \quad (2.11)$$

with the eigenvalues given as

$$\mathcal{E}_1 = \left\{ \frac{1}{2}(\delta_2 - \delta_3), \frac{1}{2}(\delta_2 + \delta_3) \right\}. \quad (2.12)$$

The  $\mathcal{M}_2$  submatrix can be constructed similarly, with the initial and final states being one of the bases  $\left\{ G^+ G^-, \frac{1}{\sqrt{2}} G^0 G^0, \frac{1}{\sqrt{2}} s_i s_i, \frac{1}{\sqrt{2}} hh, \frac{1}{\sqrt{2}} s_i s_i \right\}$  and is given by

$$\mathcal{M}_2 = \begin{pmatrix} \lambda & \frac{1}{\sqrt{2}}\lambda & \frac{1}{\sqrt{2}}(\delta_2 - \delta_3) & \frac{1}{\sqrt{2}}\lambda & \frac{1}{\sqrt{2}}(\delta_2 + \delta_3) \\ \frac{1}{\sqrt{2}}\lambda & 3\lambda & \delta_2 - \delta_3 & \lambda & \delta_2 + \delta_3 \\ \frac{1}{\sqrt{2}}(\delta_2 - \delta_3) & \delta_2 - \delta_3 & 3(d_1 + d_2 - d_3) & \delta_2 - \delta_3 & -3d_1 + d_2 \\ \frac{1}{\sqrt{2}}\lambda & \lambda & \delta_2 - \delta_3 & 3\lambda & \delta_2 + \delta_3 \\ \frac{1}{\sqrt{2}}(\delta_2 + \delta_3) & \delta_2 + \delta_3 & -3d_1 + d_2 & \delta_2 + \delta_3 & 3(d_1 + d_2 + d_3) \end{pmatrix}, \quad (2.13)$$

and the eigenvalues  $\mathcal{E}_2$  have been found by numerically solving the characteristic polynomial of order five.

The third submatrix  $\mathcal{M}_3$  can be constructed considering the basis  $\{hG^0, s_r s_i\}$  which is given by

$$\mathcal{M}_3 = \begin{pmatrix} \frac{1}{2}\lambda & 0 \\ 0 & \frac{1}{2}(-3d_1 + d_2) \end{pmatrix}, \quad (2.14)$$

and the eigenvalues are given by

$$\mathcal{E}_3 = \left\{ \frac{1}{2}\lambda, \frac{1}{2}(-3d_1 + d_2) \right\}. \quad (2.15)$$

The submatrix  $\mathcal{M}_4$  consists of singly charged channels with ingoing and outgoing states as any of the following sets  $\{hG^+, s_r G^+, G^0 G^+, s_i G^+\}$  and is given by

$$\mathcal{M}_4 = \begin{pmatrix} \frac{1}{2}\lambda & 0 & 0 & 0 \\ 0 & \frac{1}{2}(\delta_2 + \delta_3) & 0 & 0 \\ 0 & 0 & \frac{1}{2}\lambda & 0 \\ 0 & 0 & 0 & \frac{1}{2}(\delta_2 - \delta_3) \end{pmatrix}, \quad (2.16)$$

with the eigenvalues as

$$\mathcal{E}_4 = \left\{ \frac{1}{2}\lambda, \frac{1}{2}(\delta_2 + \delta_3), \frac{1}{2}(\delta_2 - \delta_3) \right\}. \quad (2.17)$$

Finally, the submatrix of the unique doubly-charged channel with the ingoing and the outgoing state as  $\frac{1}{\sqrt{2}}G^+G^+$  is given by

$$\mathcal{M}_5 = 2\lambda. \quad (2.18)$$

To achieve unitarity, the absolute values of all the eigenvalues (all the components of  $\mathcal{E}_1, \mathcal{E}_2, \mathcal{E}_3, \mathcal{E}_4$  and  $\mathcal{E}_5$ ) of these submatrices should be less than  $8\pi$ .

**Vacuum stability :** The constraints arise from ensuring that the scalar potential given in Eq. 2.1 is bounded from below (BFB) from all field directions. The copositivity criteria [30, 31] have been used to determine the BFB conditions. Taking into account only the quartic terms, the potential can be written in terms of charged ( $G^+$ ) and neutral components ( $\phi^0, S$ ) of the scalar fields and is given by

$$V_0^{(4)}(G^+, \phi^0, S) = \frac{1}{4} \left[ \lambda \left( \phi^{0*2} \phi^{02} + 2\phi^0 \phi^{0*} G^+ G^- + G^{+2} G^{-2} \right) + 2\delta_3 |S|^2 G^+ G^- + (d_1 + d_2 + d_3) |S|^4 \right], \quad (2.19)$$

which can be expressed in the form of  $V_0^{(4)} = \Phi^\dagger \mathcal{A} \Phi$  where  $\Phi = (G^+ \ \phi^0 \ S)^\top$  and  $\mathcal{A}$  is known as the copositive matrix. We found that all the 2-field BFB conditions are subsets of the 3-field BFB conditions and are given by

$$\left\{ \lambda \geq 0, d_{123} \geq 0, \lambda d_{123} \geq 0, \delta_3 + \sqrt{\lambda d_{123}} \geq 0, \delta_3 + \sqrt{2\lambda d_{123} + 2\delta_3 \sqrt{\lambda d_{123}}} + \sqrt{\lambda d_{123}} \geq 0 \right\}. \quad (2.20)$$

**Perturbativity :** Demanding that the model remain perturbative across any scale imposes the following conditions

$$|\lambda| < 4\pi, |\delta_2| < 4\pi, |\delta_3| < 4\pi, |d_1| < 4\pi, |d_2| < 4\pi, |d_3| < 4\pi. \quad (2.21)$$

Along with the theoretical constraints, there are additional relevant experimental results that severely constrain the BSM parameter space in various extended scalar scenarios,

which are discussed in the following.

**Electroweak precision tests :** The oblique electroweak parameters [32, 33], namely the parameters  $S, T$  and  $U$ , encode the corrections in the propagator of the EW gauge bosons, which can put stringent constraints on many extended scalar scenarios. In the presence of non-vanishing vevs of the singlet in cxSM, the singlet fields provide non-negligible quantum corrections to the self energies of  $W^\pm$  and  $Z$  bosons via mixing with the SM Higgs doublet. The parameters  $S, T$ , and  $U$  can be expressed in terms of the physical masses and mixing angles of our model and are given by

$$S = \frac{1}{24\pi} \left[ (c_1^2 c_2^2 - 1) (\log(M_1^2) + G(M_1^2, m_Z^2)) + s_1^2 c_2^2 (\log(M_2^2) + G(M_2^2, m_Z^2)) + s_2^2 (\log(M_3^2) + G(M_3^2, m_Z^2)) \right], \quad (2.22)$$

$$T = \frac{3}{16\pi s_W^2 m_W^2} \left[ (c_1^2 c_2^2 - 1) (F(m_Z^2, M_1^2) - F(m_W^2, M_1^2)) + s_1^2 c_2^2 (F(m_Z^2, M_2^2) - F(m_W^2, M_2^2)) + s_2^2 (F(m_Z^2, M_3^2) - F(m_W^2, M_3^2)) \right], \quad (2.23)$$

$$U = \frac{1}{24\pi} \left[ (c_1^2 c_2^2 - 1) (G(M_1^2, m_Z^2) - G(M_1^2, m_W^2)) + s_1^2 c_2^2 (G(M_2^2, m_Z^2) - G(M_2^2, m_W^2)) + s_2^2 (G(M_3^2, m_Z^2) - G(M_3^2, m_W^2)) \right], \quad (2.24)$$

where the functions  $G(x, y)$  and  $F(x, y)$  are defined as

$$G(x, y) = -\frac{79}{3} + 9\frac{x}{y} - 2\frac{x^2}{y^2} + \left( -10 + 18\frac{x}{y} - 6\frac{x^2}{y^2} + \frac{x^3}{y^3} - 9\frac{x-y}{x+y} \right) \log \frac{x}{y} + \frac{1}{y} \left( 12 - 4\frac{x}{y} + \frac{x^2}{y^2} \right) f(x, x^2 - 4xy), \quad (2.25)$$

$$F(x, y) = \left[ \frac{x+y}{2} - \frac{xy}{x-y} \log \frac{x}{y} \right] (1 - \delta_{xy}), \quad (2.26)$$

$$f(x, y) = \sqrt{y} \log \left| \frac{x - \sqrt{y}}{x + \sqrt{y}} \right| \Theta(y) + 2\sqrt{-y} \tan^{-1} \frac{\sqrt{-y}}{x} \Theta(-y), \quad (2.27)$$

with  $\delta_{ij}$  and  $\Theta$  are the Kronecker delta and the Heaviside theta function, respectively. The results of the fit to the electroweak precision data are [34]

$$S \equiv \hat{S} + \sigma_S = 0.05 \pm 0.11; T \equiv \hat{T} + \sigma_T = 0.09 \pm 0.13; U \equiv \hat{U} + \sigma_U = 0.01 \pm 0.11, \quad (2.28)$$

with the correlation coefficients as

$$\rho_{ST} = 0.90; \rho_{TU} = -0.83; \rho_{SU} = -0.59. \quad (2.29)$$

We construct the test statistic  $\chi^2 = X^\top \mathcal{C}^{-1} X$  with  $X = (S - \hat{S} \quad T - \hat{T} \quad U - \hat{U})^\top$  with the covariance matrix given as

$$\mathcal{C} = \begin{pmatrix} \sigma_S^2 & \rho_{ST}\sigma_S\sigma_T & \rho_{SU}\sigma_S\sigma_U \\ \rho_{ST}\sigma_S\sigma_T & \sigma_T^2 & \rho_{TU}\sigma_T\sigma_U \\ \rho_{SU}\sigma_S\sigma_U & \rho_{TU}\sigma_T\sigma_U & \sigma_U^2 \end{pmatrix}, \quad (2.30)$$

and put constraints on the parameter space at 95% confidence interval utilizing  $\chi^2 \leq 6.18$ .

**Higgs observables :** The mixing angles of the BSM scalars with Higgs, i.e.  $\theta_2$  and  $\theta_3$ , can be constrained from direct scalar searches and precision Higgs measurements at the LHC [35]. The scalar mixing angles considered in our analysis lie well within the experimental upper bound reported in [36, 37] for additional scalars in the absence of any  $\mathcal{Z}_2$  symmetry.

All the aforementioned theoretical as well as experimental constraints were implemented during the numerical scan to find the parameter space resulting in SFOPT. We now proceed to discuss the construction of the effective potential for the cxSM model, which is the key ingredient for analyzing the dynamics of phase transitions.

### 3 Phase transition

In the presence of additional scalar fields, SFOPT can be achieved, unlike in the case of SM. In order to study the dynamics of cosmological phase transitions, the key ingredient is the effective thermal potential, which comprises one-loop thermal corrections to the zero-temperature potential. In this section, we delve into the details of the effective potential and present the parameter space that exhibits SFOPT along with several benchmark points.

#### 3.1 Effective potential

The construction of a one-loop effective thermal potential contains quantum corrections at finite temperature, which can be decomposed into a zero temperature correction known as the Coleman-Weinberg potential ( $V_{\text{CW}}$ ) [38] and the temperature dependent part denoted as  $V_T$ . The CW contribution to the tree level potential in the Landau gauge<sup>1</sup> is given by

$$V_{\text{CW}} = \frac{1}{64\pi^2} \sum_j (-1)^{F_j} n_j M_j^4 \left[ \log \frac{M_j^2(H_i)}{\mu^2} - C_j + C_\epsilon \right] \quad (3.1)$$

in the  $\overline{\text{MS}}$  scheme where  $M_j$  is the field dependent mass of the  $j$ -th particle with  $n_j$  degrees of freedom. The constant  $C_j = 3/2$  ( $5/6$ ) for scalars and fermions (gauge bosons), whereas the overall sign is determined by  $F_j = 0$  and  $F_j = 1$  for bosons and fermions, respectively. The renormalization scale has been set at the value of the top mass, i.e.,  $\mu \simeq 173$  GeV. The divergent part of the CW potential, denoted as  $C_\epsilon = 2/\epsilon - \gamma + 4\pi$  can be absorbed by introducing the counter terms given by

$$\begin{aligned} V_{\text{CT}} = & -\frac{1}{2}\delta\mu_H^2 H^\dagger H + \frac{1}{4}\delta\lambda (H^\dagger H)^2 + \left( \delta a S + \frac{1}{4}\delta b_1 S^2 + \text{h.c.} \right) + \frac{1}{2}\delta b_2 |S|^2 \\ & + \left( \frac{1}{6}\delta\mu_3 S^3 + \delta\tilde{\mu}_3 |S|^2 S + \text{h.c.} \right) + \left( \frac{1}{8}\delta d_1 S^4 + \frac{1}{8}\delta d_3 |S|^2 S^2 + \text{h.c.} \right) + \frac{1}{4}\delta d_2 |S|^4. \quad (3.2) \\ & + H^\dagger H \left[ \left( \frac{1}{4}\delta\delta_1 S + \frac{1}{4}\delta\delta_3 S^2 + \text{h.c.} \right) + \frac{1}{2}\delta\delta_2 |S|^2 \right] \end{aligned}$$

<sup>1</sup>The gauge independent analysis of effective potential remains beyond the scope of this work; for details, see Ref. [39, 40]

where the coefficients are explicitly given in Appendix B by fixing the following renormalization conditions given by

$$\frac{\partial (V_{\text{CW}} + V_{\text{CT}})}{\partial x} = 0; \quad \frac{\partial^2 (V_{\text{CW}} + V_{\text{CT}})}{\partial x \partial y} = 0, \quad (3.3)$$

evaluated at the vacuum configuration given in Eq. 2.4 where  $x, y \in \{h, s_r, s_i\}$ , ensuring that the tree level masses and vevs of the scalars remain unaltered.

The one loop temperature dependent part of the effective potential is given by [41, 42]

$$V_T(H_i, T) = \frac{T^4}{2\pi^2} \left[ \sum_B n_B J_B \left( \frac{M_B^2(H_i)}{T^2} \right) + \sum_F n_F J_F \left( \frac{M_B^2(H_i)}{T^2} \right) \right] \quad (3.4)$$

where the bosonic and fermionic functions are denoted by  $J_B(x)$  and  $J_F(x)$  respectively and are given by

$$J_{B/F}(x^2) = \int_0^\infty k^2 \log \left[ 1 \mp e^{-\sqrt{x^2+k^2}} \right] dk \quad (3.5)$$

where the negative (positive) sign appears for the bosons (fermions). In the high temperature regime ( $T \gg M_i$ ), these functions can be expanded in the following form given by

$$\begin{aligned} J_B(x^2) &= -\frac{\pi^4}{45} + \frac{\pi^2}{12}x^2 - \frac{\pi}{6}x^3 + \mathcal{O}(x^4), \\ J_F(x^2) &= \frac{7\pi^4}{360} - \frac{\pi^2}{24}x^2 + \mathcal{O}(x^4). \end{aligned} \quad (3.6)$$

with  $x \equiv M_i/T$ . It should be noted that bosonic and fermionic functions suffer from infrared divergences arising from Matsubara-zero modes [43], which can be taken care of by their corresponding thermal masses via daisy resummation. We implement this method in the Arnold-Espinosa scheme [44] by considering the following additional daisy contributions to the effective potential given by

$$V_{\text{ring}}(H_i, T) = - \sum_j \frac{n_j T}{12\pi} \left[ (M_j^2(H_i) + \Pi_j T^2)^{3/2} - M_j^3(H_i) \right], \quad (3.7)$$

where  $\Pi$  is the diagonal matrix containing all the daisy coefficients, which can be read off from the high-temperature expansion of  $V_T(H_i, T)$  and are given by

$$\begin{bmatrix} \frac{2\delta_2 + 6\lambda}{48} + \frac{3g_2^2 + g_1^2}{16} + \frac{3(y_b^2 + y_t^2) + y_\tau^2}{12} & 0 & 0 \\ 0 & \frac{4d_2 + 3d_3 + 4(\delta_2 + \delta_3)}{48} & 0 \\ 0 & 0 & \frac{4d_2 - 3d_3 + 4(\delta_2 - \delta_3)}{48} \end{bmatrix}. \quad (3.8)$$

Thus, combining all the contributions discussed above, the total effective potential is given by

$$V_{\text{eff}}(H_i, T) = V_0(H_i) + V_{\text{CW}}(H_i) + V_{\text{CT}} + V_T(H_i, T) + V_{\text{ring}}(H_i, T). \quad (3.9)$$

The critical temperature ( $T_C$ ) of a phase transition is defined as the temperature at which the symmetric phase and the broken phase coexist, and it can be obtained by equating the potential at the field values of these two different phases [45, 46]. The strength of an FOPT is determined by the parameter  $\gamma$ , which in our case is defined as

$$\gamma = \sqrt{\sum_{i=1}^3 \gamma_i^2} = \sqrt{\sum_{i=1}^3 \left(\frac{\Delta H_i}{T_C}\right)^2} \quad (3.10)$$

where  $\gamma_i$  is the individual strength defined as the ratio of the difference in vevs of the scalar field ( $\Delta H_i$ ) and the critical temperature  $T_C$ . The criterion [42] for SFOPT is chosen as  $\gamma \geq 1$ .

In cosmological phase transitions, in addition to the critical temperature, another temperature is of significant importance, which is the bubble nucleation temperature ( $T_N$ ), which is generally lower than  $T_C$ . The transition proceeds through the nucleation of bubbles of the true vacuum within the false vacuum. The probability of tunneling from the false to the true vacuum per unit volume at a finite temperature  $T$  is given by [47],

$$\Gamma(T) = T^4 \left(\frac{S_3}{2\pi T}\right)^{3/2} e^{-S_3/T}, \quad (3.11)$$

where  $S_3$  is the three-dimensional Euclidean action evaluated for the bounce solution and is given by

$$S_3 = 4\pi \int r^2 dr \left[ \frac{1}{2} \left(\frac{dH_i}{dr}\right)^2 + V_{\text{eff}}(H_i, T) \right], \quad (3.12)$$

and the field  $H_i$  follow the Euclidean equation of motion [48, 49] given by

$$\frac{d^2 H_i}{dr^2} + \frac{2}{r} \frac{dH_i}{dr} = \frac{\partial V_{\text{eff}}(H_i, T)}{\partial H_i}, \quad (3.13)$$

with the boundary conditions  $dH_i/dr = 0$  at  $r = 0$  and  $H_i = 0$  as  $r \rightarrow \infty$ . The nucleation temperature can be obtained by satisfying the following condition [48]

$$\frac{S_3(T_N)}{T_N} \simeq 140. \quad (3.14)$$

We now present our parameter space scan and study of the various benchmark points presented in Table 2.

### 3.2 Scan based analysis

We implement the cxSM model in `PhaseTracer2` [50, 51] to find the latent heat released ( $\alpha$ ) during SFOPT, the inverse duration ( $\beta$ ), and the nucleation temperature ( $T_N$ ) of the transition, which are essential quantities for the generation of GW as discussed later. We choose a hierarchical scenario for the BSM scalar masses ( $M_3 > M_2$ ) along with their vevs at  $\mathcal{O}(100)$  GeV with other dimension full parameters below the electroweak scale. We perform an extensive numerical scan over the input parameters given in Eq. 2.10 in the

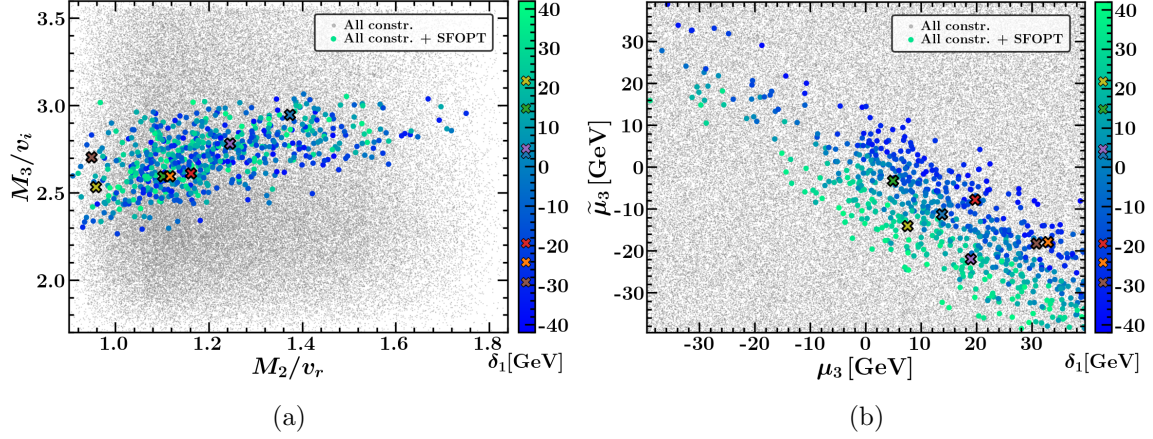


**Figure 1:** Parameter space satisfying SFOPT in the cxSM. The gray points are allowed by all the constraints, while the colored points exhibit SFOPT. The colored markers denote the benchmark points for which the details are presented in Table 2.

Parameter	Range	Parameter	Range	Parameter	Range
$M_2$ [GeV]	[150, 300]	$v_r$ [GeV]	[100, 200]	$\delta_1$ [GeV]	[-40, 40]
$M_3$ [GeV]	[150, 300]	$v_i$ [GeV]	[50, 150]	$\mu_3$ [GeV]	[-40, 40]
$\sin \theta_\alpha$	[-0.2, 0.2]	$a$ [GeV <sup>3</sup> ]	[-100, 100]	$\tilde{\mu}_3$ [GeV]	[-40, 40]

**Table 1:** Ranges of the parameters for the numerical scan where  $\alpha = 1, 2, 3$ .

		$M_2$	$M_3$	$\sin \theta_1$	$\sin \theta_2$	$\sin \theta_3$	$v_r$	$v_i$	$a$	$\delta_1$	$\mu_3$	$\tilde{\mu}_3$
		[GeV]	[GeV]				[GeV]	[GeV]	[GeV <sup>3</sup> ]	[GeV]	[GeV]	[GeV]
BP1	✖	220.225	290.731	$1.608 \times 10^{-1}$	$-4.779 \times 10^{-3}$	$-7.376 \times 10^{-2}$	189.554	111.256	38.427	-19.312	19.744	-7.691
BP2	✖	198.053	279.991	$-1.744 \times 10^{-1}$	$5.288 \times 10^{-2}$	$-1.158 \times 10^{-1}$	179.670	107.939	3.460	14.754	4.849	-3.180
BP3	✖	204.300	269.592	$-2.626 \times 10^{-2}$	$1.133 \times 10^{-1}$	$-1.183 \times 10^{-1}$	147.990	91.482	61.965	16.280	11.781	-11.181
BP4	✖	206.234	264.191	$-8.856 \times 10^{-2}$	$5.183 \times 10^{-5}$	$8.578 \times 10^{-2}$	184.632	101.817	89.160	-24.132	32.857	-17.904
BP5	✖	207.945	275.466	$-1.044 \times 10^{-1}$	$8.611 \times 10^{-2}$	$1.115 \times 10^{-1}$	167.078	98.955	77.440	4.587	18.881	-21.893
BP6	✖	183.971	232.786	$1.060 \times 10^{-1}$	$6.085 \times 10^{-2}$	$-1.588 \times 10^{-2}$	194.042	86.067	-78.745	-29.185	30.787	-18.232
BP7	✖	183.658	267.481	$-5.518 \times 10^{-2}$	$-5.337 \times 10^{-2}$	$-1.232 \times 10^{-1}$	191.677	105.541	-18.386	21.760	7.529	-14.066

**Table 2:** Numerical values of all the input parameters as listed in Eq. 2.10 for the benchmark points exhibiting SFOPT. The colored marker in the second column refers to the corresponding benchmark point shown in Fig. 1.

ranges specified in Table 1 to find out the regions of parameter space exhibiting SFOPT while agreeing with all the constraints discussed earlier.

We present the parameter space in Fig. 1 where the colored points satisfy SFOPT. Although the mixing angles were uniformly distributed in the specified ranges as mentioned

			$T_C$ [GeV]	$T_N$ [GeV]	$\gamma$	$\alpha/10^{-3}$	$\beta/H_N$
BP1	✖	I	151.593	139.498	1.317	5.412	2861.602
BP2	✘	I	169.232	156.956	1.259	1.656	4088.654
		II	150.843	146.301	0.926	1.862	6728.672
BP3	✙	I	163.703	149.986	1.170	1.952	3159.387
		II	149.586	144.535	0.974	2.108	5927.351
BP4	✚	I	134.191	120.798	1.567	9.348	2008.619
BP5	✛	I	125.918	77.716	2.128	77.639	140.406
BP6	✜	I	137.017	117.730	1.691	11.840	1283.953
BP7	✝	I	145.081	126.023	1.585	9.362	1466.208

**Table 3:** Relevant parameters of phase transition for the benchmark points of Table 2. The third column refers to a particular step in the case of a multistep phase transition.

in Table 1, we observe that the region satisfying SFOPT lies within the range of  $M_2/v_r \in [0.9, 1.7]$  and  $M_3/v_i \in [2.25, 3.0]$  along with a negative correlation between the self cubic couplings  $\mu_3$  and  $\tilde{\mu}_3$ . We find single step as well as multistep SFOPT along different field directions, which are categorized in three major types, which we proceed to discuss via several benchmark points (denoted by coloured ✖ in Fig. 1 and shown in Table 2) in the following section.

### 3.3 Types

From our numerical analysis, we analyze the dynamics of SFOPT via several benchmark points and majorly classify them in three categories, where SFOPT occurs in the direction of the BSM (along  $H_2$  and/or  $H_3$  only), the SM (along  $H_1$  only), and both SM + BSM (along  $H_1$  and  $H_2/H_3$ ).

We first discuss the benchmark points where the SFOPT occurs only in the direction of BSM scalars, i.e, along the  $H_2$  or  $H_3$  direction. As can be seen from the phase structure for the first benchmark point BP1 shown in Fig. 2a, there is an SFOPT only along the  $H_2$  direction at  $T_C = 156.31$  GeV. This can be explicitly verified from the change in the fields given by  $\Delta H_1 \simeq 123$  GeV,  $\Delta H_2 \simeq 157$  GeV,  $\Delta H_3 \simeq 8$  GeV resulting to individual strengths of  $\gamma_1 = 0.79$ ,  $\gamma_2 = 1.04$ ,  $\gamma_3 = 0.06$  respectively, leading to a combined strength of  $\gamma = 1.32$ . The discontinuity of the field values is associated with a single step first order transition at the critical temperature, denoted by the vertical dashed gray line distinguishing the boundary between the symmetric phase and the broken phase. The bubbles of true vacuum start to nucleate at slightly lower temperature with  $T_N = 139.5$  GeV as indicated by the vertical purple dashed line in Fig. 2a. The phase diagram has been represented in the  $H_1 - H_2, H_2 - H_3$  and  $H_1 - H_3$  space with the arrow explicitly denoting the discontinuity of the fields, as shown in Fig. 2b. In contrast to BP1, there can be phase transitions realized in multiple steps, out of which the first step exhibits SFOPT as shown in Figs. 3a and 3b

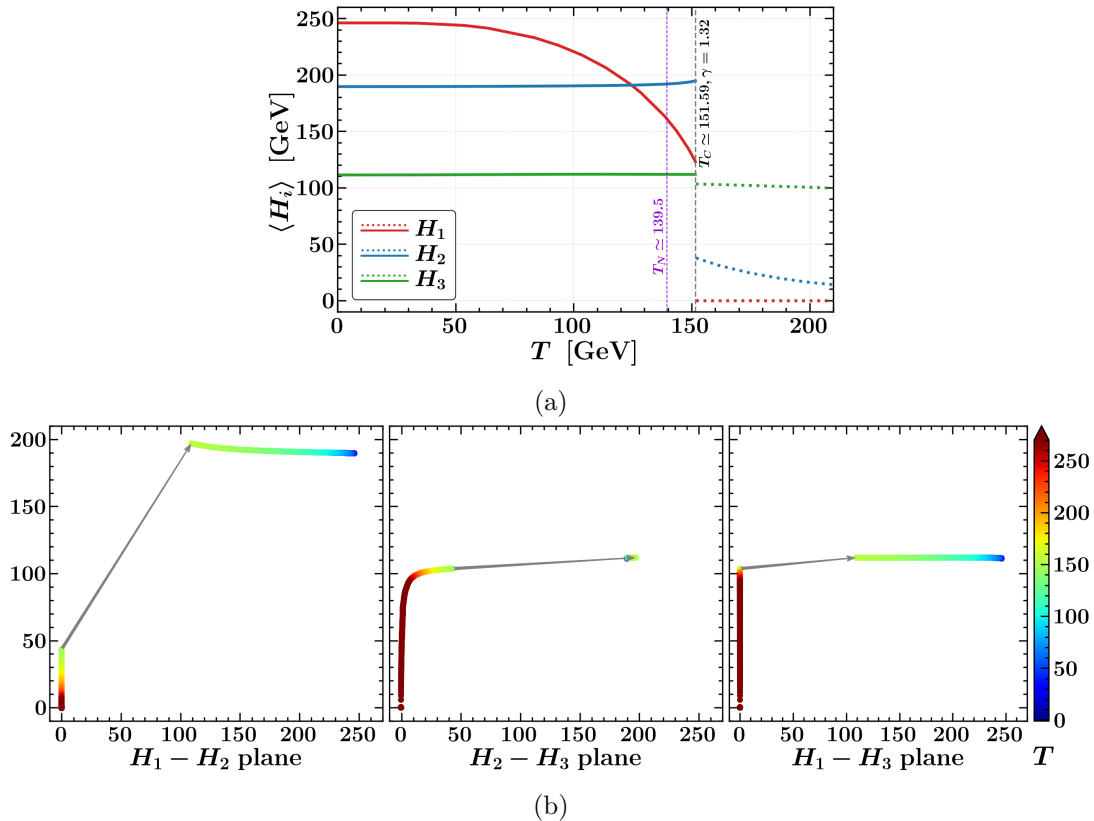


**Figure 2:** Upper panel (2a) shows the evolution of all the fields as a function of temperature for BP1, where the different phases are denoted via solid and dashed lines. The vertical dashed gray and purple lines denote the critical and nucleation temperatures, respectively. Lower panel (2b) depicts the phase diagram for BP1 in the three different field spaces, while temperature has been shown parametrically in the color bar with the arrows denoting the discontinuity of fields at the critical temperature. The numerical values of all the fields and temperature shown in the figures are in the units of GeV.

for BP2 and BP3, respectively. The benchmark point BP2 (BP3) exhibits an SFOPT in the first step along the  $H_2$  direction at  $T_C = 169.23$  (164.12) GeV with  $\gamma = 1.26$  (1.16), whereas the second transition is a weak FOPT along all field directions.

Next, we identify the benchmark point BP4 where a single step SFOPT occurs only in the direction of SM Higgs, i.e.,  $\gamma_1 > 1$ , as shown in Fig. 4a. The critical temperature is found to be  $T_C = 134.19$  GeV with a total strength of  $\gamma = 1.57$ , whereas the nucleation temperature is found to be  $T_N = 120.8$  GeV. The fields  $H_1$  and  $H_2$  exhibit a discontinuity at the critical temperature, whereas the field  $H_3$  is continuous throughout the false and true vacuum.

Finally, we discuss the SFOPT achieved along both the SM and the BSM field directions. The evolution of the fields is shown in Fig. 4b where it is evident that both  $\gamma_1$  and  $\gamma_2$  are greater than unity, leading to a relatively larger combined strength of  $\gamma = 2.13$  evaluated at the critical temperature of  $T_C = 125.92$  GeV. The evolution of fields for the

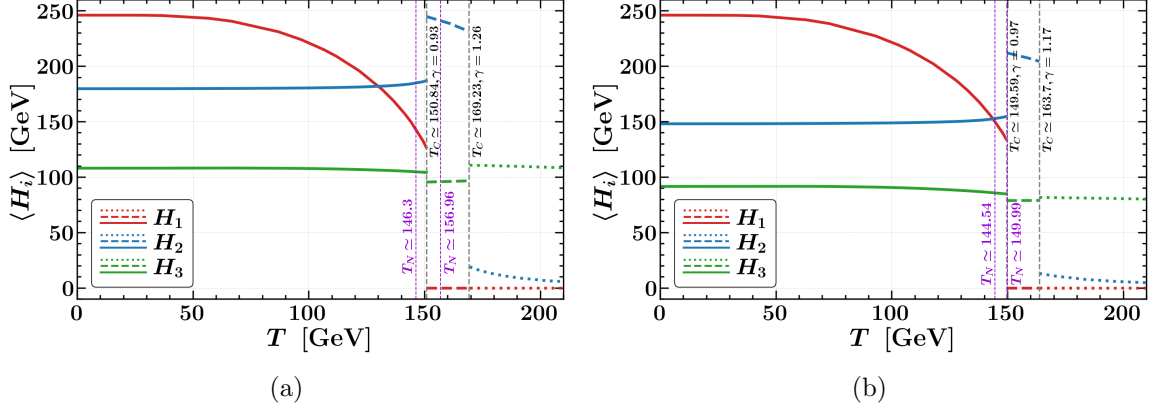


Figure 3: Same as Fig. 2a for BP2 (left panel) and BP3 (right panel).

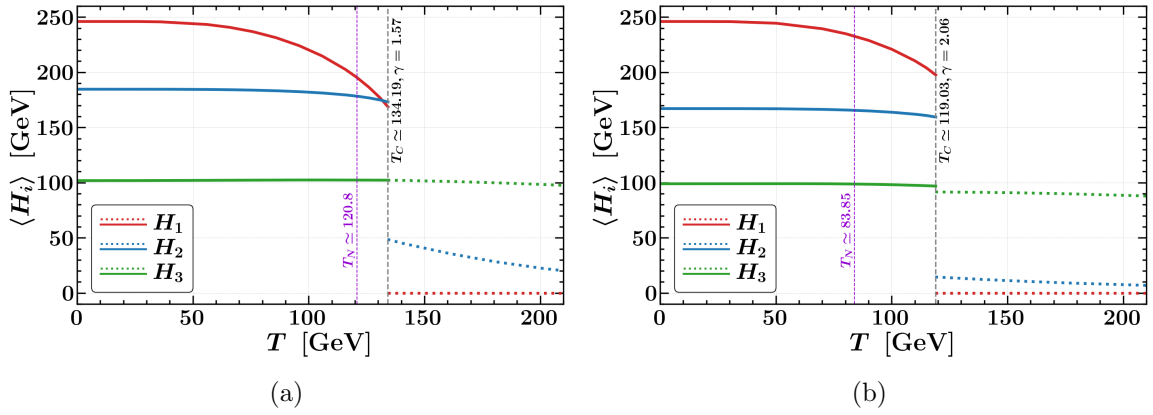


Figure 4: Same as Fig. 2a for BP4 (left panel) and BP5 (right panel).

benchmark points BP6 and BP7 is similar in nature to the details given in Table 2.

## 4 Gravitational waves

Cosmological SFOPT in the early Universe can serve as a source of gravitational waves which carry imprints of high-energy physics operating at scales far beyond the reach of collider searches, providing a complementary probe into the thermal history of the Universe. These GWs are stochastic in nature, with three dominant mechanisms contributing to this GW background being [52, 53]

1. **Bubble collisions** : During an SFOPT, bubbles of the true vacuum nucleate and expand within the false vacuum. Their subsequent collisions partially convert the released vacuum energy into gravitational waves, especially in cases of runaway walls or vacuum transitions.
2. **Acoustic waves** : The expanding bubble walls induce coherent motion in the surrounding plasma, generating long-lasting sound waves that efficiently source gravita-

tional waves. This mechanism usually determines the peak frequency of the GW in first order thermal phase transitions.

3. **Magnetohydrodynamic (MHD) turbulence:** After the acoustic phase, the plasma motion becomes turbulent and can sustain magnetic fields, leading to an additional subdominant contribution to the stochastic GW background.

In general, all three mechanisms act simultaneously, and the resulting contribution to the stochastic GW background can be written as [54]

$$\Omega_{\text{GW}}h^2 \simeq \Omega_{\text{coll}}h^2 + \Omega_{\text{sw}}h^2 + \Omega_{\text{turb}}h^2, \quad (4.1)$$

where the terms correspond to the contributions from bubble collisions, sound waves, and magnetohydrodynamic turbulence, respectively. The shape and amplitude of the resulting GW spectrum are governed by a few key macroscopic parameters characterizing the phase transition

- $\alpha$  : measures the transition strength through the vacuum energy released,
- $\beta/H_N$  : quantifies the inverse duration of the transition in units of the Hubble expansion rate at the nucleation epoch,
- $T_N$  : the nucleation temperature as defined in Eq. 3.14,
- $v_w$  : the velocity of the bubble wall that determines the efficiency of energy transfer to the plasma.

In this work, we focus on the *runaway bubble wall* scenario assuming  $v_w \simeq 1$ , which maximizes the energy available for GW production. Among these parameters,  $\alpha$  is proportional to the latent heat evolved during the phase transition. It also signifies the strength of the phase transition defined as [55]

$$\alpha = \frac{\epsilon(T_N)}{\rho_R(T_N)}, \quad (4.2)$$

where  $\epsilon$  denotes the released vacuum energy density given by

$$\epsilon(T_N) = \Delta V_{\text{eff}} - T \left. \frac{d\Delta V_{\text{eff}}}{dT} \right|_{T=T_N}. \quad (4.3)$$

It also signifies the strength of the phase transition defined as the ratio of released vacuum energy density ( $\epsilon$ ) and total energy density of the radiation dominated Universe ( $\rho_R$ ) at nucleation temperature defined as [55]

$$\alpha = \frac{\epsilon(T_N)}{\rho_R(T_N)} = \frac{\Delta V_{\text{eff}} - T \frac{d\Delta V_{\text{eff}}}{dT}}{\frac{\pi^2}{30} g_*(T) T^4} \Bigg|_{T=T_N}, \quad (4.4)$$

where  $\Delta V_{\text{eff}}$  corresponds to the difference between the effective potential values in the false and true vacuum, with  $g_*$  representing the number of relativistic degrees of freedom. The radiation energy density at the nucleation temperature is given by

$$\rho_R(T_N) = \frac{\pi^2 g_*(T_N) T_N^4}{30}, \quad (4.5)$$

with  $g_*$  representing the number of relativistic degrees of freedom.

The parameter  $\beta$  quantifies the inverse time scale of the phase transition relative to the Hubble expansion rate at nucleation ( $H_N$ ) and is given by [56]

$$\frac{\beta}{H_N} = T \left. \frac{d(S_3/T)}{dT} \right|_{T=T_N}, \quad (4.6)$$

and the contribution of bubble collisions [57] in the GW spectrum within the envelope approximation, considering thin-wall bubbles, is given by

$$\Omega_{\text{coll}} h^2 = 1.67 \times 10^{-5} \frac{0.48 v_w^3}{1 + 5.3 v_w^2 + 5 v_w^4} \left( \frac{100}{g_*(T_N)} \right)^{\frac{1}{3}} \left( \frac{H_N}{\beta} \right)^2 \left( \frac{\kappa_\phi \alpha}{1 + \alpha} \right)^2 S_{\text{env}} \left( \frac{f}{f_{\text{env}}} \right), \quad (4.7)$$

where  $\kappa_\phi$  is the efficiency factor that determines the fraction of the vacuum energy converted to the kinetic energy of the wall,  $S_{\text{env}}$  is the spectral shape with  $f_{\text{env}}$  being the peak frequency of the spectrum, and are given by

$$\kappa_\phi = \frac{1}{1 + 0.715\alpha} \left[ 0.715\alpha + \frac{4}{27} \sqrt{\frac{3\alpha}{2}} \right], \quad (4.8)$$

$$S_{\text{env}}(r) = (0.064 r^{-3} + 0.456 r^{-1} + 0.48 r)^{-1}, \quad (4.9)$$

$$\frac{f_{\text{env}}}{1 \mu\text{Hz}} = 16.5 \left( \frac{0.35}{1 + 0.069 v_w + 0.69 v_w^4} \right) \left( \frac{g_*(T_N)}{100} \right)^{\frac{1}{6}} \left( \frac{\beta}{H_N} \right) \left( \frac{T_N}{100 \text{ GeV}} \right). \quad (4.10)$$

Numerical simulations [57, 58] have shown that the efficiency of GW production from pure bubble collisions is relatively small once the plasma is included, since most of the bubble-wall energy is transferred to the surrounding fluid rather than remaining in the scalar field gradient. Consequently,  $\Omega_{\text{coll}}$  typically gives a subdominant contribution in realistic thermal phase transitions.

The contribution of sound waves in the GW spectrum redshifted to the present day Universe can be written as [59]

$$\Omega_{\text{sw}} h^2 = 0.025 F_{\text{gw},0} \left( \frac{\kappa_{\text{sw}} \alpha}{1 + \alpha} \right)^2 S_{\text{sw}} \left( \frac{f}{f_{\text{sw}}} \right) \min \left[ \frac{H_N R_N}{\bar{U}_f}, 1 \right] (H_N R_N) h^2, \quad (4.11)$$

where  $F_{\text{gw},0} = 3.57 \times 10^{-5} (100/g_*(T_N))^{1/3}$ ,  $\kappa_{\text{sw}}$  is the efficiency factor,  $\bar{U}_f$  is the enthalpy-weighted root mean square of the fluid velocity and the mean bubble radius is given by  $R_N = (8\pi)^{1/3} (v_w/\beta)$  at the nucleation temperature [50]. The spectral shape and peak frequency are respectively given by

$$S_{\text{sw}}(r) = r^3 \left( \frac{7}{4 + 3r^2} \right)^{7/2} \quad (4.12)$$

$$\frac{f_{\text{sw}}}{1 \mu\text{Hz}} = 2.6 \left( \frac{T_N}{100 \text{ GeV}} \right) \left( \frac{g_*(T_N)}{100} \right)^{\frac{1}{6}} \left( \frac{1}{H_N R_N} \right). \quad (4.13)$$

The dominant source of gravitational waves usually arises from long-lasting acoustic (sound) waves in the plasma. During bubble expansion and collision, the kinetic energy of the walls

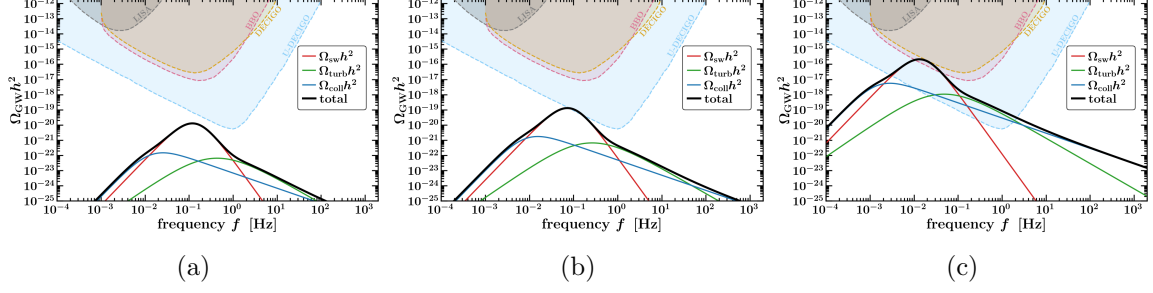


**Figure 5:** The stochastic GW spectrum for BP1 (left panel), BP4 (middle panel) and BP5 (right panel). Individual contributions for each benchmark point from sound wave, magnetohydrodynamic turbulence, and bubble collisions are shown in red, green, and blue solid lines corresponding to Eq. 4.11, 4.14, and 4.7 respectively. The dashed gray, violet, yellow, and light blue lines correspond to the sensitivity curves for LISA, BBO, DECIGO, and U-DECIGO respectively.

is efficiently transferred to the surrounding fluid, producing bulk motion and coherent sound waves that persist for about a Hubble time after the transition. Since these sound waves last much longer than the brief collision phase, they typically dominate the total gravitational wave energy density in most electroweak-scale first-order phase transitions.

The part of the GW spectrum resulting from the MHD turbulence, redshifted to today, is given by [60]

$$\Omega_{\text{turb}} h^2 = 3.35 \times 10^{-4} v_w \left( \frac{H_N}{\beta} \right) \left( \frac{\kappa_{\text{turb}} \alpha}{1 + \alpha} \right)^{3/2} \left( \frac{100}{g_*(T_N)} \right)^{1/3} \frac{(f/f_{\text{turb}})^3}{(1 + f/f_{\text{turb}})^{11/3} (1 + 8\pi f/H_0)}, \quad (4.14)$$

where  $\kappa_{\text{turb}}$  is chosen to be a small fraction of  $\kappa_{\text{sw}}$  [61]. The peak frequency and the red-shifter Hubble rate at the production of GWs are respectively given by

$$\frac{f_{\text{turb}}}{1 \mu\text{Hz}} = 27 \frac{1}{v_w} \left( \frac{\beta}{H_N} \right) \left( \frac{T_N}{100 \text{GeV}} \right) \left( \frac{g_*(T_N)}{100} \right)^{1/6}, \quad (4.15)$$

$$H_0 = 16.5 \left( \frac{g_*(T_N)}{100} \right)^{1/6} \left( \frac{T_N}{100 \text{GeV}} \right) \mu\text{Hz}. \quad (4.16)$$

The contribution arising from magnetohydrodynamic (MHD) turbulence is generated in the plasma once the acoustic waves become non-linear and turbulent. A small fraction of the fluid kinetic energy cascades into turbulent vortices and possibly magnetic fields, which can further source stochastic GWs [62]. This component is typically suppressed compared to the sound-wave term, since only a minor fraction of the bulk kinetic energy is converted into turbulence. Nevertheless, it can enhance the high-frequency tail of the spectrum and is relevant for probing small-scale plasma dynamics.

In our analysis, we show three GW spectrums corresponding to each type, which are strong FOPT along the SM, BSM, and both directions, respectively. Figs. 5a, 5b, 5c show the individual contribution of each term of Eq. 4.1 corresponding to each benchmark of

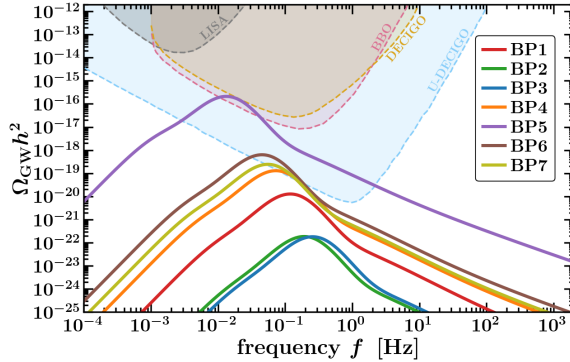


**Figure 6:** GW spectrum for all the benchmark points with the sensitivity curves for different experiments.

each type of phase transition i.e BP1, BP4 and BP5 respectively. As expected, the acoustic contribution is the highest, the collision contribution is higher in the lower frequency side, while that of MHD is higher in the higher frequencies. The physical reason is that, during a first-order phase transition, the expanding bubble walls interact strongly with the surrounding relativistic plasma, transferring most of their energy into bulk fluid motion rather than remaining as scalar-field gradients [53]. Unlike the long-lived acoustic source, gravitational waves from bubble collisions are produced only for a brief moment during the overlap of expanding walls. The turbulence in the plasma that follows contributes at higher frequencies but carries a comparatively small and rapidly fading share of the released energy.

Finally, we show the GW spectrum for all the benchmark points in Fig. 6. The peak of the GW spectrum is highest for BP5, followed by BP7 and then BP6, where SFOPT is observed along both directions. GW spectrum due to BP4 corresponds to the case where SFOPT is observed only along the SM direction with a lower peak than that of BP5, BP6, and BP7, as expected. Similarly, for the spectrum corresponding to the BSM directions, the peak is highest for BP1, followed by BP3, and then BP2, and they are even lower than that of the SM case. This is due to the combined effect of the strength of the phase transition  $\alpha$  and the inverse duration of the phase transition  $\beta/H_N$  as can be verified from Table 3. Almost all GW spectra corresponding to the benchmarks where SFOPT is observed along both directions can be detected in the upcoming BBO, DECIGO, and U-DECIGO detectors.

## 5 Conclusion and discussion

In this paper, we have revisited one of the simplest extensions to the Standard Model by incorporating a complex singlet scalar, without imposing any extra discrete or continuous global symmetries on this scalar singlet field. This approach allows for a fully general treatment of the scalar potential, enabling richer possibilities in the vacuum structure. Specifically, it allows a configuration where both the real and imaginary components of the

singlet acquire vevs alongside the Standard Model Higgs field, leading to a more intricate interplay among the scalars.

We first imposed various theoretical and experimental constraints on the parameters of the full scalar potential. To explore the thermal history of the early Universe, we have calculated the finite temperature effective potential at the one-loop level, incorporating daisy resummation and counter terms. This framework enabled us to investigate the electroweak phase transition dynamics across all three relevant field directions—the Higgs and the two singlet components. Adopting a hierarchical mass spectrum for the physical scalars to align with phenomenological viability, we have conducted a comprehensive parameter scan over the model’s 11 free parameters. This effort identified viable regions of the parameter space capable of supporting a strong first-order phase transition (SFOPT), a key ingredient for successful electroweak baryogenesis and the generation of observable gravitational waves. We have classified the phase transitions based on the primary field directions involved in the SFOPT, resulting in three distinct categories: those dominated by the Standard Model direction, those along the beyond-Standard-Model singlet directions, and hybrid cases involving both. To illustrate these behaviors, we have chosen a few representative benchmark points, some of which exhibit multi-step transitions characterized by sequential symmetry breaking at different critical temperatures, with vev-to-temperature ratios exceeding unity at the critical temperature, confirming the strength of the transitions. Through our scan of the model parameter space, we have shown some insightful patterns: SFOPT tends to occur in regimes where the ratios of the masses of the heavier scalars to their corresponding singlet vevs are close to order one. More precisely, the parameter space favors  $M_2/v_r$  falling between approximately 1.0 and 1.5 for the real singlet component, and  $M_3/v_i$  between 2.25 and 3.0 for the imaginary part, highlighting the delicate balance required between mass scales and couplings.

Furthermore, we have computed the stochastic gravitational wave spectra arising from bubble nucleation and related dynamics in these benchmark scenarios. The spectra are shaped by contributions from sound waves in the plasma, magnetohydrodynamic turbulence, and bubble wall collisions, with the sound wave component often dominating because of efficient energy transfer in relativistic fluids. Particularly, the gravitational wave signals from points featuring SFOPT along both Standard Model and beyond-Standard-Model directions exhibit peak amplitudes and frequencies that intersect the projected sensitivity curves of advanced detectors like DECIGO, as well as potentially BBO and U-DECIGO. This overlap suggests that such signals could be detectable in the near future, providing a complementary probe to collider experiments and opening a new window into high-energy physics beyond the Standard Model.

Overall, the SM augmented with a complex singlet scalar scenario appears to be a versatile and minimal framework that not only addresses shortcomings in the Standard Model, such as the baryon asymmetry, but also predicts testable multimessenger signatures. Future work could extend this analysis to incorporate CP violation mechanisms for full baryogenesis calculations or explore collider signatures of the additional scalars to further constrain the viable parameter space.

## Acknowledgments

RP would like to thank Peter Athron, Andrew Fowlie, and Yang Zhang for helping with the use of `PhaseTracer2` and Sougata Ganguly for various discussions. DM and KM acknowledge the financial support provided by the Indian Association for the Cultivation of Science (IACS), Kolkata.

## A Lagrangian parameters in terms of physical quantities

Here we show the functional dependence of quartic couplings mentioned in the tree-level potential given in Eq. 2.1 in terms of physical mass eigenvalues, mixing angles, and vevs. Utilizing the tadpole equations given in 2.5, 2.6 and 2.7 the quartic couplings can be expressed as

$$\lambda = \frac{2}{v_h^2} A, \quad (\text{A-1})$$

$$\delta_2 = \frac{1}{4v_h v_r v_i} \left( 4Bv_i + 4Cv_r - \sqrt{2}v_h v_i \delta_1 \right), \quad (\text{A-2})$$

$$\delta_3 = \frac{1}{4v_h v_r v_i} \left( 4Bv_i - 4Cv_r - \sqrt{2}v_h v_i \delta_1 \right), \quad (\text{A-3})$$

$$d_1 = \frac{1}{96v_i^2 v_r^3} \left[ 24\sqrt{2}a_1 v_i^2 + 2\sqrt{2}\tilde{\mu}_3 v_i^2 (v_r^2 + v_i^2) - 6\sqrt{2}\mu_3 v_i^2 (v_i^2 + 5v_r^2) + 3(8Dv_i^2 v_r - 16Ev_i v_r^2 + 8Fv_r^3 + \sqrt{2}v_h^2 v_i^2 \delta_1) \right], \quad (\text{A-4})$$

$$d_2 = \frac{1}{96} \left[ \frac{72F}{v_i^2} + \frac{72D}{v_r^2} + \frac{48E + 2\sqrt{2}(3\mu_3 - 13\tilde{\mu}_3)v_i}{v_i v_r} + \frac{3\sqrt{2}}{v_r^3} (24a + 2(-3\mu_3 + \tilde{\mu}_3)v_i^2 + 3v_h^2 \delta_1) \right], \quad (\text{A-5})$$

$$d_3 = -\frac{F}{v_r^2} + \frac{D}{v_r^2} - \frac{\mu_3 + \tilde{\mu}_3}{2\sqrt{2}v_r} + \frac{1}{12\sqrt{2}v_r^3} (24a + 2(-3\mu_3 + \tilde{\mu}_3)v_i^2 + 3v_h^2 \delta_1), \quad (\text{A-6})$$

where

$$\begin{aligned} A &= M_1^2 c_2^2 c_3^2 + M_2^2 (c_3 s_1 s_2 + c_1 s_3)^2 + M_3^2 (c_1 c_3 s_2 - s_1 s_3)^2, \\ B &= (M_3^2 - M_2^2) \cos(2\theta_3) c_1 s_1 s_2 + c_1^2 c_3 (M_3^2 s_2^2 - M_2^2) s_3 + c_3 (M_1^2 c_2^2 + s_1^2 (M_2^2 s_2^2 - M_3^2)) s_3, \\ C &= c_2 (c_3 (M_1^2 - M_3^2 c_1^2 - M_2^2 s_1^2) s_2 + (-M_2^2 + M_3^2) c_1 s_1 s_3), \\ D &= M_1^2 c_2^2 s_3^2 + M_3^2 (c_3 s_1 + c_1 s_2 s_3)^2 + M_2^2 (c_1 c_3 - s_1 s_2 s_3)^2, \\ E &= c_2 ((M_2^2 - M_3^2) c_1 c_3 s_1 + (M_1^2 - M_3^2 c_1^2 - M_2^2 s_1^2) s_2 s_3), \\ F &= c_2^2 (M_3^2 c_1^2 + M_2^2 s_1^2) + M_1^2 s_2^2. \end{aligned} \quad (\text{A-7})$$

## B Counter terms in the effective potential

Utilizing the renormalization condition mentioned in Eq. 3.3, we fix the coefficients of the counter terms given in Eq. 3.2 and are given by

$$\delta\mu_H^2 = \frac{1}{v_h^2 v_i^3} \left[ -v_h v_i^3 \left( -3V_{\text{CW}}^h + v_h V_{\text{CW}}^{h,h} + v_i V_{\text{CW}}^{h,s_i} \right) - v_i^3 v_r \left( 2V_{\text{CW}}^{s_r} + v_h V_{\text{CW}}^{h,s_r} - 2v_r V_{\text{CW}}^{s_r,s_r} \right) \right]$$

$$+ 2v_r^4 (V_{\text{CW}}^{s_i} - v_i V_{\text{CW}}^{s_i, s_i}) \Big], \quad (\text{B-1})$$

$$\delta\lambda = \frac{2}{v_h^3} \left[ V_{\text{CW}}^h - v_h V_{\text{CW}}^{h, h} \right], \quad (\text{B-2})$$

$$\delta\delta_1 = \frac{4\sqrt{2}}{v_h^2 v_i^3} \left[ -v_i^3 V_{\text{CW}}^{s_r} + v_i^3 v_r V_{\text{CW}}^{s_r, s_r} + v_r^3 (V_{\text{CW}}^{s_i} - v_i V_{\text{CW}}^{s_i, s_i}) \right] \quad (\text{B-3})$$

$$\delta\delta_2 = \frac{1}{v_h^2 v_i^3 v_r} \left[ v_i^3 (2V_{\text{CW}}^{s_r} - v_h V_{\text{CW}}^{h, s_r}) - v_i^2 v_r (v_h V_{\text{CW}}^{h, s_i} + 2v_i V_{\text{CW}}^{s_r, s_r}) - 2v_r^3 (V_{\text{CW}}^{s_i} - v_i V_{\text{CW}}^{s_i, s_i}) \right], \quad (\text{B-4})$$

$$\delta\delta_3 = \frac{1}{v_h^2 v_i^3 v_r} \left[ v_i^3 (2V_{\text{CW}}^{s_r} - v_h V_{\text{CW}}^{h, s_r}) + v_i^2 v_r (v_h V_{\text{CW}}^{h, s_i} - 2v_i V_{\text{CW}}^{s_r, s_r}) - 2v_r^3 (V_{\text{CW}}^{s_i} - v_i V_{\text{CW}}^{s_i, s_i}) \right], \quad (\text{B-5})$$

$$\delta b_1 = \frac{1}{2v_i^2 v_r} \left[ v_i^3 (-2V_{\text{CW}}^{s_r} + v_h V_{\text{CW}}^{h, s_r} + v_i V_{\text{CW}}^{s_r, s_i}) - v_i^2 v_r (-3V_{\text{CW}}^{s_i} + v_h V_{\text{CW}}^{h, s_i} + v_i V_{\text{CW}}^{s_i, s_i}) - v_i^2 v_r^2 V_{\text{CW}}^{s_r, s_i} + v_r^3 (-V_{\text{CW}}^{s_i} + v_i V_{\text{CW}}^{s_i, s_i}) \right], \quad (\text{B-6})$$

$$\delta b_2 = \frac{1}{2v_i^3 v_r} \left[ v_i^3 (-2V_{\text{CW}}^{s_r} + v_h V_{\text{CW}}^{h, s_r} + v_i V_{\text{CW}}^{s_r, s_i}) + v_i^2 v_r (-3V_{\text{CW}}^{s_i} + v_h V_{\text{CW}}^{h, s_i} + v_i V_{\text{CW}}^{s_i, s_i}) + v_i^2 v_r^2 V_{\text{CW}}^{s_r, s_i} + v_r^3 (-V_{\text{CW}}^{s_i} + v_i V_{\text{CW}}^{s_i, s_i}) \right], \quad (\text{B-7})$$

$$\delta d_1 = \frac{1}{2v_i^3 v_r} \left[ v_i^2 V_{\text{CW}}^{s_r, s_i} + v_r V_{\text{CW}}^{s_i} - v_i v_r V_{\text{CW}}^{s_i, s_i} \right], \quad (\text{B-8})$$

$$\delta d_2 = \frac{1}{2v_i^3 v_r} \left[ -v_i^2 V_{\text{CW}}^{s_r, s_i} + 3v_r V_{\text{CW}}^{s_i} - 3v_i v_r V_{\text{CW}}^{s_i, s_i} \right], \quad (\text{B-9})$$

with the shorthand notation of the partial derivatives given as

$$V_{\text{CW}}^x \equiv \frac{\partial V_{\text{CW}}}{\partial x}; \quad V_{\text{CW}}^{x, y} \equiv \frac{\partial^2 V_{\text{CW}}}{\partial x \partial y}, \quad (\text{B-10})$$

has been used where  $x, y \in \{h, s_r, s_i\}$ . Without an adequate number of renormalization conditions, all other counter terms appearing in Eq. 3.2 have been chosen to be equal to zero.

## References

- [1] PLANCK collaboration, *Planck 2018 results. VI. Cosmological parameters*, *Astron. Astrophys.* **641** (2020) A6 [[1807.06209](#)].
- [2] A. D. Sakharov, *Violation of CP Invariance, C asymmetry, and baryon asymmetry of the universe*, *Pisma Zh. Eksp. Teor. Fiz.* **5** (1967) 32.
- [3] K. Kajantie, M. Laine, K. Rummukainen and M. E. Shaposhnikov, *Is there a hot electroweak phase transition at  $m_H \gtrsim m_W$ ?*, *Phys. Rev. Lett.* **77** (1996) 2887 [[hep-ph/9605288](#)].
- [4] F. Csikor, Z. Fodor and J. Heitger, *Endpoint of the hot electroweak phase transition*, *Phys. Rev. Lett.* **82** (1999) 21 [[hep-ph/9809291](#)].

- [5] M. Dine, R. G. Leigh, P. Y. Huet, A. D. Linde and D. A. Linde, *Towards the theory of the electroweak phase transition*, *Phys. Rev. D* **46** (1992) 550 [[hep-ph/9203203](#)].
- [6] M. Trodden, *Electroweak baryogenesis*, *Rev. Mod. Phys.* **71** (1999) 1463 [[hep-ph/9803479](#)].
- [7] D. E. Morrissey and M. J. Ramsey-Musolf, *Electroweak baryogenesis*, *New J. Phys.* **14** (2012) 125003 [[1206.2942](#)].
- [8] J. van de Vis, J. de Vries and M. Postma, *Bubble Trouble: a Review on Electroweak Baryogenesis*, [2508.09989](#).
- [9] J. Baker et al., *The Laser Interferometer Space Antenna: Unveiling the Millihertz Gravitational Wave Sky*, [1907.06482](#).
- [10] J. Crowder and N. J. Cornish, *Beyond LISA: Exploring future gravitational wave missions*, *Phys. Rev. D* **72** (2005) 083005 [[gr-qc/0506015](#)].
- [11] G. M. Harry, P. Fritschel, D. A. Shaddock, W. Folkner and E. S. Phinney, *Laser interferometry for the big bang observer*, *Class. Quant. Grav.* **23** (2006) 4887.
- [12] N. Seto, S. Kawamura and T. Nakamura, *Possibility of direct measurement of the acceleration of the universe using 0.1-Hz band laser interferometer gravitational wave antenna in space*, *Phys. Rev. Lett.* **87** (2001) 221103 [[astro-ph/0108011](#)].
- [13] S. Kawamura et al., *Current status of space gravitational wave antenna DECIGO and B-DECIGO*, *PTEP* **2021** (2021) 05A105 [[2006.13545](#)].
- [14] J. R. Espinosa and M. Quiros, *The Electroweak phase transition with a singlet*, *Phys. Lett. B* **305** (1993) 98 [[hep-ph/9301285](#)].
- [15] S. Profumo, M. J. Ramsey-Musolf and G. Shaughnessy, *Singlet Higgs phenomenology and the electroweak phase transition*, *JHEP* **08** (2007) 010 [[0705.2425](#)].
- [16] J. Braathen, S. Heinemeyer, C. P. Boatella and A. Verduras Schaeidt, *Complementarity of gravitational wave analyses and di-Higgs production in the exploration of the Electroweak Phase Transition dynamics in the  $R_{\chi}SM$* , [2510.12569](#).
- [17] J. Ellis, M. Lewicki, M. Merchand, J. M. No and M. Zych, *The scalar singlet extension of the Standard Model: gravitational waves versus baryogenesis*, *JHEP* **01** (2023) 093 [[2210.16305](#)].
- [18] V. Vaskonen, *Electroweak baryogenesis and gravitational waves from a real scalar singlet*, *Phys. Rev. D* **95** (2017) 123515 [[1611.02073](#)].
- [19] S. Lee, D. Kim, J.-H. Cho, J. Kim and J. Song, *Multistep strong first-order electroweak phase transitions in the inverted type-I 2HDM: Parameter space, gravitational waves, and collider phenomenology*, *Phys. Rev. D* **112** (2025) 055035 [[2506.03260](#)].
- [20] D. K. Ghosh, K. Mukherjee and S. Mukherjee, *Electroweak phase transition in two scalar singlet model with  $pNGB$  dark matter*, *JHEP* **01** (2025) 078 [[2409.00192](#)].
- [21] A. Biswas and S. Ganguly, *Probing low scale leptogenesis through gravitational wave*, [2505.01820](#).
- [22] V. Keus, L. Lewitt and J. Thomson-Cooke, *Electroweak phase transition enhanced by a CP-violating dark sector*, [2511.04636](#).
- [23] O. Karkout, A. Papaefstathiou, M. Postma, G. Tetlalmatzi-Xolocotzi, J. van de Vis and T. du Pree, *Triple Higgs boson production and electroweak phase transition in the two-real-singlet model*, *JHEP* **11** (2024) 077 [[2404.12425](#)].

- [24] S. Guan, H.-K. Guo, D. Jiao, Q. Liang, L. Wu and Y. Zhang, *Measuring Gravitational Wave Spectrum from Electroweak Phase Transition and Higgs Self-Couplings*, [2511.00996](#).
- [25] E. Fernández-Martínez, J. López-Pavón, J. M. No, T. Ota and S. Rosauero-Alcaraz,  *$\nu$  Electroweak baryogenesis: the scalar singlet strikes back*, *Eur. Phys. J. C* **83** (2023) 715 [[2210.16279](#)].
- [26] R. Pramanick, T. S. Ray and A. Shaw, *Neutrino mass and leptogenesis in a hybrid seesaw model with a spontaneously broken CP*, *JHEP* **06** (2023) 099 [[2211.04403](#)].
- [27] V. Barger, P. Langacker, M. McCaskey, M. Ramsey-Musolf and G. Shaughnessy, *Complex Singlet Extension of the Standard Model*, *Phys. Rev. D* **79** (2009) 015018 [[0811.0393](#)].
- [28] J. R. Espinosa, T. Konstandin and F. Riva, *Strong Electroweak Phase Transitions in the Standard Model with a Singlet*, *Nucl. Phys. B* **854** (2012) 592 [[1107.5441](#)].
- [29] B. W. Lee, C. Quigg and H. B. Thacker, *Weak Interactions at Very High-Energies: The Role of the Higgs Boson Mass*, *Phys. Rev. D* **16** (1977) 1519.
- [30] K. Kannike, *Vacuum Stability Conditions From Copositivity Criteria*, *Eur. Phys. J. C* **72** (2012) 2093 [[1205.3781](#)].
- [31] J. Chakraborty, P. Konar and T. Mondal, *Copositive Criteria and Boundedness of the Scalar Potential*, *Phys. Rev. D* **89** (2014) 095008 [[1311.5666](#)].
- [32] M. E. Peskin and T. Takeuchi, *A New constraint on a strongly interacting Higgs sector*, *Phys. Rev. Lett.* **65** (1990) 964.
- [33] W. Grimus, L. Lavoura, O. M. Ogreid and P. Osland, *The Oblique parameters in multi-Higgs-doublet models*, *Nucl. Phys. B* **801** (2008) 81 [[0802.4353](#)].
- [34] GFITTER GROUP collaboration, *The global electroweak fit at NNLO and prospects for the LHC and ILC*, *Eur. Phys. J. C* **74** (2014) 3046 [[1407.3792](#)].
- [35] S. D. Lane, I. M. Lewis and M. Sullivan, *Resonant multiscalar production in the generic complex singlet model in the multi-TeV region*, *Phys. Rev. D* **110** (2024) 055017 [[2403.18003](#)].
- [36] I. M. Lewis, J. Scott, M. A. S. Alcaraz and M. Sullivan, *Real Singlet Scalar Benchmarks in the Multi-TeV Resonance Regime*, [2410.08275](#).
- [37] T. Robens and R. Santos, *BSM: Extended Scalar Sectors*, 7, 2025, [2507.21910](#).
- [38] S. R. Coleman and E. J. Weinberg, *Radiative Corrections as the Origin of Spontaneous Symmetry Breaking*, *Phys. Rev. D* **7** (1973) 1888.
- [39] N. K. Nielsen, *On the Gauge Dependence of Spontaneous Symmetry Breaking in Gauge Theories*, *Nucl. Phys. B* **101** (1975) 173.
- [40] R. Fukuda and T. Kugo, *Gauge Invariance in the Effective Action and Potential*, *Phys. Rev. D* **13** (1976) 3469.
- [41] L. Dolan and R. Jackiw, *Symmetry Behavior at Finite Temperature*, *Phys. Rev. D* **9** (1974) 3320.
- [42] M. Quiros, *Finite temperature field theory and phase transitions*, in *ICTP Summer School in High-Energy Physics and Cosmology*, pp. 187–259, 1, 1999, [hep-ph/9901312](#).
- [43] T. Matsubara, *A New approach to quantum statistical mechanics*, *Prog. Theor. Phys.* **14** (1955) 351.

- [44] P. B. Arnold and O. Espinosa, *The Effective potential and first order phase transitions: Beyond leading-order*, *Phys. Rev. D* **47** (1993) 3546 [[hep-ph/9212235](#)].
- [45] H. H. Patel and M. J. Ramsey-Musolf, *Baryon Washout, Electroweak Phase Transition, and Perturbation Theory*, *JHEP* **07** (2011) 029 [[1101.4665](#)].
- [46] H. H. Patel and M. J. Ramsey-Musolf, *Stepping Into Electroweak Symmetry Breaking: Phase Transitions and Higgs Phenomenology*, *Phys. Rev. D* **88** (2013) 035013 [[1212.5652](#)].
- [47] A. D. Linde, *Decay of the False Vacuum at Finite Temperature*, *Nucl. Phys. B* **216** (1983) 421.
- [48] K. Enqvist, J. Ignatius, K. Kajantie and K. Rummukainen, *Nucleation and bubble growth in a first order cosmological electroweak phase transition*, *Phys. Rev. D* **45** (1992) 3415.
- [49] I. Affleck, *Quantum Statistical Metastability*, *Phys. Rev. Lett.* **46** (1981) 388.
- [50] P. Athron, C. Balazs, A. Fowlie, L. Morris, W. Searle, Y. Xiao et al., *PhaseTracer2: from the effective potential to gravitational waves*, *Eur. Phys. J. C* **85** (2025) 559 [[2412.04881](#)].
- [51] P. Athron, C. Balázs, A. Fowlie and Y. Zhang, *PhaseTracer: tracing cosmological phases and calculating transition properties*, *Eur. Phys. J. C* **80** (2020) 567 [[2003.02859](#)].
- [52] C. Caprini et al., *Science with the space-based interferometer eLISA. II: Gravitational waves from cosmological phase transitions*, *JCAP* **04** (2016) 001 [[1512.06239](#)].
- [53] C. Caprini et al., *Detecting gravitational waves from cosmological phase transitions with LISA: an update*, *JCAP* **03** (2020) 024 [[1910.13125](#)].
- [54] J. Ellis, M. Lewicki and J. M. No, *Gravitational waves from first-order cosmological phase transitions: lifetime of the sound wave source*, *JCAP* **07** (2020) 050 [[2003.07360](#)].
- [55] M. Kamionkowski, A. Kosowsky and M. S. Turner, *Gravitational radiation from first order phase transitions*, *Phys. Rev. D* **49** (1994) 2837 [[astro-ph/9310044](#)].
- [56] A. Nicolis, *Relic gravitational waves from colliding bubbles and cosmic turbulence*, *Class. Quant. Grav.* **21** (2004) L27 [[gr-qc/0303084](#)].
- [57] R. Jinno and M. Takimoto, *Gravitational waves from bubble collisions: An analytic derivation*, *Phys. Rev. D* **95** (2017) 024009 [[1605.01403](#)].
- [58] S. J. Huber and T. Konstandin, *Gravitational Wave Production by Collisions: More Bubbles*, *JCAP* **09** (2008) 022 [[0806.1828](#)].
- [59] M. Hindmarsh, S. J. Huber, K. Rummukainen and D. J. Weir, *Shape of the acoustic gravitational wave power spectrum from a first order phase transition*, *Phys. Rev. D* **96** (2017) 103520 [[1704.05871](#)].
- [60] P. Binetruy, A. Bohe, C. Caprini and J.-F. Dufaux, *Cosmological Backgrounds of Gravitational Waves and eLISA/NGO: Phase Transitions, Cosmic Strings and Other Sources*, *JCAP* **06** (2012) 027 [[1201.0983](#)].
- [61] M. Hindmarsh, S. J. Huber, K. Rummukainen and D. J. Weir, *Numerical simulations of acoustically generated gravitational waves at a first order phase transition*, *Phys. Rev. D* **92** (2015) 123009 [[1504.03291](#)].
- [62] C. Caprini, R. Durrer and G. Servant, *The stochastic gravitational wave background from turbulence and magnetic fields generated by a first-order phase transition*, *JCAP* **12** (2009) 024 [[0909.0622](#)].